Appl Phys A (2009) 96: 161–169
DOI 10.1007/s00339-008-4979-z

Applied Physics A
Materials Science & Processing

INVITED PAPER

Imaging and spectroscopy of defects in semiconductors using aberration-corrected STEM

Klaus van Benthem · Stephen J. Pennycook

Received: 6 January 2008 / Accepted: 4 November 2008 / Published online: 11 December 2008
© Springer-Verlag 2008

Abstract The distribution of single dopant or impurity atoms can dramatically alter the properties of semiconductor materials. The sensitivity to detect and localize such single atoms has been greatly improved by the development of aberration correctors for scanning transmission electron microscopes. Today, electron probes with diameters well below 1 Å are available thanks to the improved electron optics. Simultaneous acquisition of image signals and electron energy-loss spectroscopy data provides means of characterization of defect structures in semiconductors with unprecedented detail. In addition to an improvement of the lateral spatial resolution, depth sensitivity is greatly enhanced because of the availability of larger probe forming angles. We report the characterization of an alternate gate dielectric interface structure. Isolated Hf atoms are directly imaged within a SiO_2 thin film formed between an HfO_2 layer and the silicon substrate. Electron energy-loss spectroscopy shows significant changes of the silicon valence state across the interface structure.

PACS 68.37.Ma · 68.37.-d · 85.30.De

K. van Benthem (✉)
Center for Nanophase Materials Sciences, Oak Ridge National Laboratory, 1 Bethel Valley Road, Oak Ridge, TN 37831, USA
e-mail: benthem@ucdavis.edu

Present address:
K. van Benthem
Department for Chemical Engineering and Materials Science, University of California at Davis, 1 Shields Ave., Davis, CA 95616, USA

S.J. Pennycook
Materials Science and Technology Division, Oak Ridge National Laboratory, 1 Bethel Valley Road, Oak Ridge, TN 37831, USA

1 Introduction

The continuing shrinkage of semiconductor devices [1, 2] with critical length scales of the order of nanometers requires a focus on their atomic structure and especially its correlation to electronic structure and macroscopic device properties. Characterization techniques are needed with resolutions and sensitivities appropriate to study critical device structures on the atomic scale. Aberration-corrected scanning transmission electron microscopy provides new capabilities to study atomic and electronic structures, chemical compositions and bonding behaviors with atomic resolution [3]. Specifically, the advent of aberration correctors that compensates for lens aberrations has enabled the formation of electron probes with diameters below 1 Å [4, 5], hence providing single atom sensitivities [6]. Furthermore, the depth of field is greatly reduced with aberration correction, and three-dimensional (3D) imaging and location of single atoms inside real device structures becomes possible. In the first half of this paper fundamental aspects of scanning transmission electron microscopy and its combination with aberration correction will be reviewed.

To keep track with the rapid scaling of transistors, the conventional SiO_2 gate dielectric layer needs to be replaced with a material characterized by a higher dielectric constant k. HfO_2 and Hf silicate thin films are promising candidates. The use of these alternate materials results in multilayer gate stacks in which a thin SiO_x layer ($x \leq 2$) is either formed spontaneously during the high-k dielectric deposition, or intentionally grown as an interlayer in contact to the substrate [7]. It has been suggested that the dielectric constant k of the SiO_x interlayer is larger than in stoichiometric bulk SiO_2 [8–10] due to inwards diffusion of Hf atoms and subsequent Hf silicate formation [8]. An alternative explanation was given by Bersuker and co-workers [9, 11] who ar-

gue that the high-k dielectric film, like, e.g., HfO_2, modifies the stoichiometry of the SiO_2 interlayer due to the higher oxygen affinity of Hf compared to Si.

The second part of the manuscript reports the assessment of the defect chemistry within the SiO_2 interlayer using aberration-corrected scanning transmission electron microscopy. In previous studies we reported the capabilities for imaging and 3D location of single Hf atoms within a chemically grown SiO_x interlayer between a polycrystalline HfO_2 film and the silicon substrate [11–13]. Other authors have thereafter reproduced the detection of single Hf atoms in the SiO_x interlayer [14–16]. In this work an intentionally grown SiO_2 thin film was used as interlayer between an HfO_2 high-k dielectric film and the substrate. The effects of the rapid thermal annealing process during the device manufacturing process on the point-defect chemistry are studied with imaging and spectroscopy techniques at atomic resolution and single atom sensitivity.

2 Scanning transmission electron microscopy

A scanning transmission electron microscope (STEM) focuses the electron beam into a fine probe, which is then scanned across an electron transparent specimen. Electrons transmitted by the specimen can simultaneously be recorded as a function of probe position by a variety of different detectors. Figure 1 shows a sketch drawing of a dedicated STEM as it was used for the current study.

Electrons scattered into high angles are collected with an annular detector. The cross-section for electrons scattered into high angles over a large angular range is roughly proportional to the squared atomic number Z of the scattering element. For large enough scattering angles, coherent effects between atomic columns average out. The scattering process itself can then be considered purely incoherent, which bypasses the phase problem that complicates interpretation of conventional high-resolution TEM using phase contrast imaging. Those electrons scattered into small angles can be collected *"on-axis"* by a bright field detector, or they can be analyzed with respect to their kinetic energy to form electron energy-loss spectra. Consequently, STEM provides the simultaneous acquisition of multiple different image and spectroscopy signals while scanning the electron probe across or pointing it directly onto different defect structures, such as point defects or interfaces.

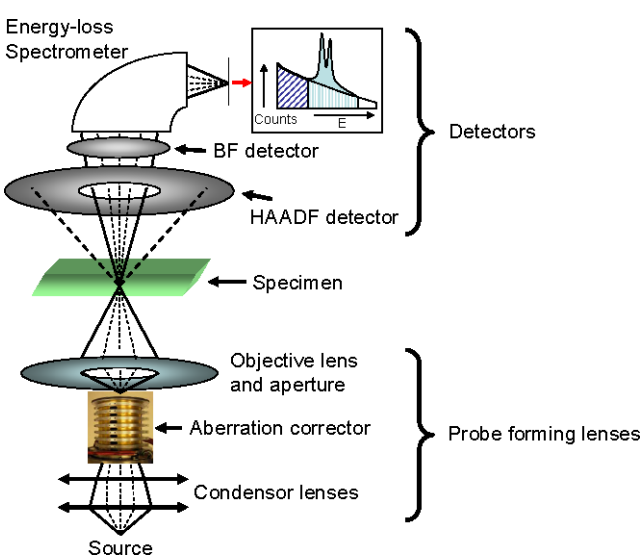

Fig. 1 Schematic drawing of the main components of an aberration-corrected dedicated scanning transmission electron microscope. The geometric setup allows simultaneous recording of different detector signals

2.1 Atomic structure investigations

The achievable spatial resolution in STEM is determined by the diameter of the electron probe, which by itself is determined by the microscope's accelerating voltage, its stability, and lens aberrations of the probe forming lenses. Aberration correctors, which are now commercially available, have enabled the formation of electron probes with diameters below 1 Å [4, 17]. Figure 2 shows two high-angle annular dark field (HAADF) images of Si in ⟨112⟩ zone axis orientation. Figure 2a was recorded with a VG Microscopes HB501 UX STEM at 100 keV showing (224) and (022) planes with a spacing of 0.91 Å. In Fig. 2b an HAADF image of the same crystal in the same orientation is shown which was recorded with a VG Microscopes HB603 U STEM operated at 300 keV. In this image, [444] lattice spacings in Si are clearly visible revealing a special resolution of 0.78 Å. The image shown in Fig. 2a was recorded by van Benthem and co-workers [18]. The micrograph in Fig. 2b was acquired by Chisholm and Nellist and is originally published in [5].

However, aberration correction not only provides higher resolution, but due to focusing the same number of electrons into a smaller area (i.e., a sharper probe), the beam current density is significantly increased compared to the uncorrected case. Therefore, signal-to-noise ratios increase quite dramatically in the experimental images. Consequently, the sensitivity is enhanced making possible the detection of single heavy atoms [6, 19].

Aberration-corrected STEM has another important, though often overlooked, advantage. The ability to use larger probe forming angles α without picking up higher-order aberrations provides a significant reduction in the optical depth of field T, following the equation

$$T = \frac{\delta_s}{\alpha} = 0.61\frac{\lambda}{\alpha^2}. \quad (1)$$

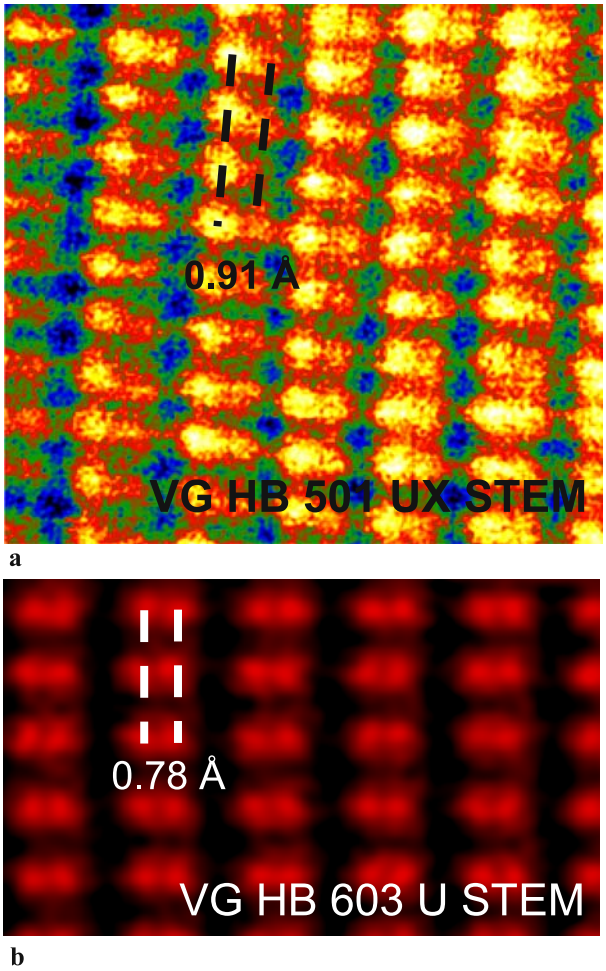

Fig. 2 High-angle annular dark field images of a single crystal of Si in ⟨112⟩ orientation. The micrographs were taken using aberration-corrected STEM instrumentation at (**a**) 100 keV [18] and (**b**) 300 keV [5], respectively

Here, δ_s is the electron probe diameter, which, in the absence of aberrations and instabilities, is given by the quotient of the electron wavelength λ and the convergence semi-angle α. Contrary to traditional transmission electron microscopy for which a large depth of field ensures a true projection view of the sample and its entire thickness, here the reduced depth of field provides increased depth sensitivity. A through-focal series acquisition can be used to optically slice the sample in a similar way as in confocal optical microscopy. The recorded stack of images can thus be used for a reconstruction of the three-dimensional microstructure of the investigated sample. A proof-of-principle experiment was published by van Benthem and co-workers [12] on the characterization of a thin HfO_2 film deposited on a silicon substrate. After rapid thermal annealing of the sample at 950°C single Hf atoms were detected inside a SiO_x interlayer, which formed during the growth process between the HfO_2 film and the substrate. By through-focal series acquisition using a 300 keV STEM the authors were able to

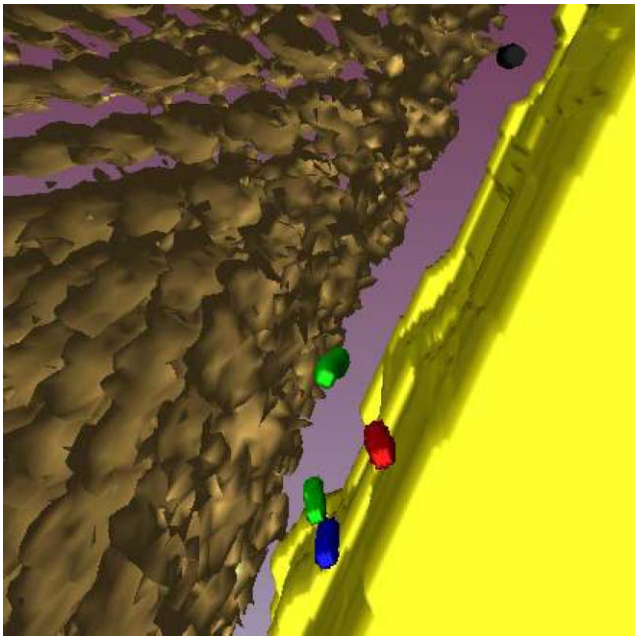

Fig. 3 Three-dimensional reconstruction obtained after through-focal series acquisition of an $HfO_2/SiO_x/Si$ multilayer system. The HfO_2 film is color-coded solid yellow. The SiO_x interlayer is not displayed, but single Hf atoms found therein are visible as cigar-shaped contrasts in different colors. Atomic columns of Si inside the substrate are visible on the left side. Reprinted with permission from K. van Benthem et al., Appl. Phys. Lett. 2005, 87, 034104. Copyright 2005, American Institute of Physics

three-dimensionally locate the position of the Hf atoms inside the oxide film and reconstruct part of the interface structure [12]. Figure 3 shows a snapshot of the reconstructed data volume illustrating the depth sensitivity.

From Fig. 3 one can observe that single atoms are reconstructed in cigar-like shapes. Furthermore, in the Si substrate area columns of Si atoms can be identified as continuous columns of intensity oriented parallel to the optical axis throughout the entire specimen thickness. These observations indicate the anisotropic spatial resolution for this 3D STEM technique. As discussed above, the lateral resolution is given by the probe diameter, i.e., typically sub-Ångström. Along the optical axis, two point objects, for instance, two single atoms, can be discriminated by a through-focal series when their vertical distance is twice the depth of field ($2T$ is typically around 7–8 nm for the 300 keV STEM) [13, 20]. Even though the through-focal series technique for obtaining 3D information reveals the highly anisotropic point-spread function, it is characterized by a higher sensitivity laterally than traditional tilt-series tomography can provide [21], so that complementary information becomes available. The tilt-series method has reached a resolution of around 1 nm in 3D, which is not sufficient to see individual atoms [22].

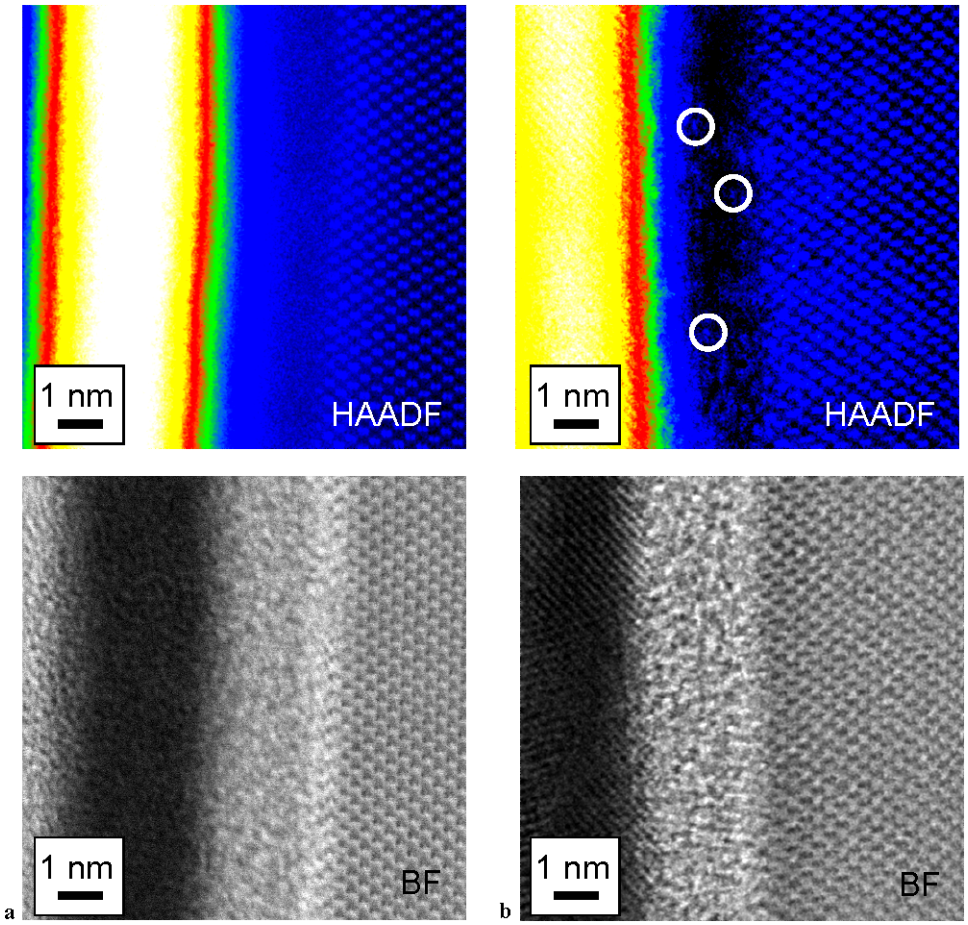

Fig. 4 HAADF and BF images taken from the $HfO_2/SiO_2/Si$ interface region before (**a**) and after (**b**) the rapid thermal annealing process. The interface plane and the ⟨110⟩ direction in Si were oriented parallel to the optical axis. The white circles mark examples of isolated Hf atoms found in the SiO_2 interlayer after annealing

2.2 Electronic structure investigations

Local electronic structures can be investigated by using electron energy-loss spectroscopy. Using a spectrometer, the inelastically scattered electrons transmitted by the sample are dispersed in energy and can thus be recorded in the form of an energy-loss spectrum. At energy losses higher than about 50 eV the spectra are dominated by absorption edges due to inner-shell excitations [23]. The corresponding energy-loss function, expressed by a double-differential cross-section $\mathrm{d}^2\sigma/\mathrm{d}\Omega\,\mathrm{d}E$, is highly localized near the atomic nuclei. In the one-electron picture, it can be written as a transition matrix element multiplied with a term taking care of energy conservation:

$$\frac{\mathrm{d}^2\sigma}{\mathrm{d}\Omega\,\mathrm{d}E} \propto \sum_{i,f} \left|\langle f|\exp(i\vec{q}\vec{r})|i\rangle\right|^2 \delta(E_f - E_i - E). \qquad (2)$$

In (2), $|i\rangle$ and $|f\rangle$ denote the initial and final states of the atomic wave-functions, respectively, and E_i and E_f are the corresponding energies of these states. $\mathrm{d}\Omega$ is the solid angle defined by the collection semi-angle β, and E is the energy-loss due to the inelastic scattering event. Upon summation over all final states the term responsible for energy conservation becomes the local density of states. Equation (2) is often referred to as the dynamic form factor (DFF) [24], which describes the near-edge fine structure of absorption edges in EELS through the unoccupied densities of states modulated by a transition matrix element (see (2)).

3 Experimental details

To study the origin of isolated Hf atoms inside manufactured gate stacks as observed in an earlier study [12], two sample materials were prepared for this study to systematically characterize isolated conditions corresponding to critical transistor fabrication process steps. Nominally 21 Å of SiO_2 were thermally grown on the Si (100) surface. In the following, this film will be referred to as a *good oxide*. Afterwards a thin HfO_2 layer with a nominal thickness of 3 nm was deposited onto the SiO_2 film using atomic layer deposition at 320°C. One of the two samples was then annealed at 1000°C for 10 s in N_2 atmosphere, representing the rapid thermal annealing process during transistor fabrication. Growth and annealing experiments were carried out

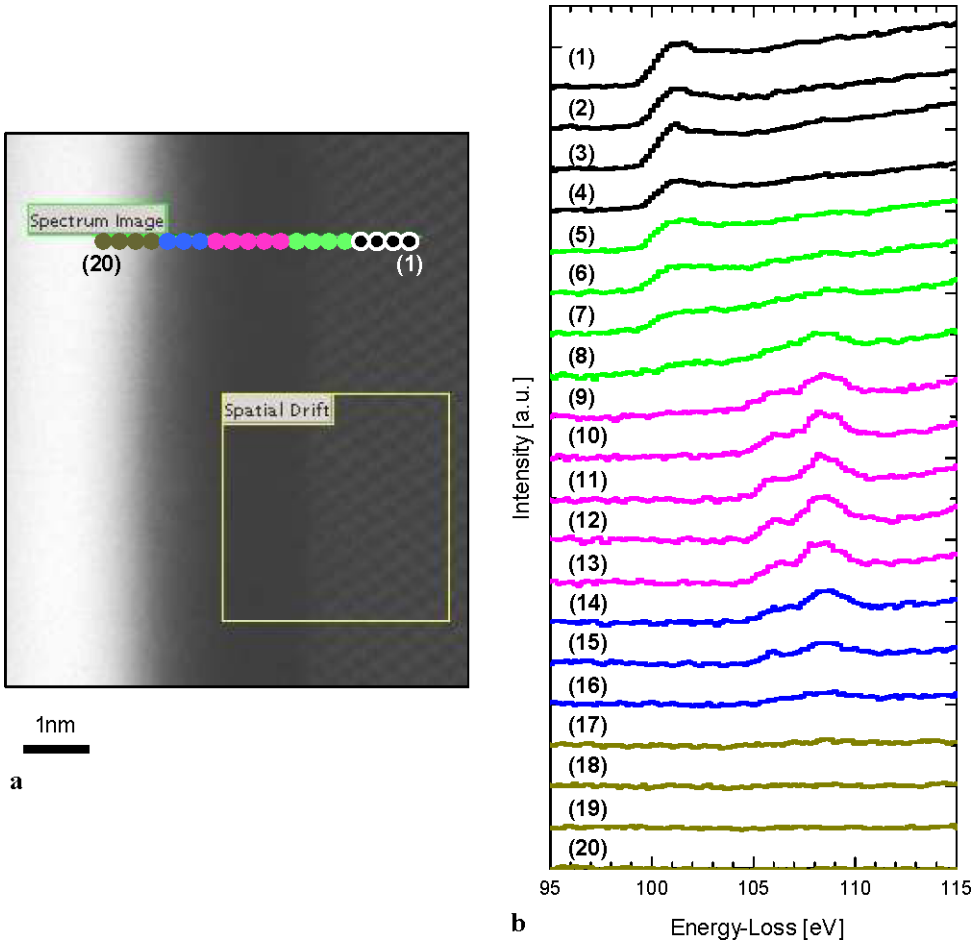

Fig. 5 HAADF survey image (**a**) of the as-deposited sample, and EELS spectra of the Si $L_{2,3}$ absorption edge (**b**) recorded along the line identified in the survey image. All spectra were channel-to-channel gain corrected and background stripped. The area marked with "Spatial Drift" was used to calculate a cross-correlation function during spectrum acquisition to correct for simultaneous specimen drift

at International Sematech at Austin, TX, USA. Details of the deposition process are reported elsewhere [11].

The so formed high-k dielectric stacks were then prepared as cross-sectional TEM samples using cutting, grinding, and wet-polishing techniques. No ion-thinning was used to avoid any preparation-induced damaging of the atomic structure [25]. Electron transparency was achieved solely by tripod-polishing.

High-resolution three-dimensional annular dark field imaging was conducted using the Oak Ridge aberration-corrected VG Microscopes HB603 U dedicated STEM operated at 300 keV. This microscope is characterized by sub-Ångström probe diameters [5], i.e., lateral resolution, and a depth of field T of 3–4 nm [6, 12, 13] corresponding to a vertical resolution $2T$ of the order of 7–8 nm [6, 13]. Electron energy-loss spectroscopy (EELS) measurements were conducted using a UHV Enfina parallel electron energy-loss spectrometer attached to the aberration-corrected VG Microscopes HB501 UX dedicated STEM operated at 100 keV. EELS data of the Si $L_{2,3}$ absorption edges were recorded as one-dimensional spectrum images (line profiles) using an energy dispersion of 0.2 eV/channel with acquisition times ranging between 0.2 s and 1.0 s per spectrum. The presented energy-loss spectra were corrected for channel-to-channel gain variations and are background subtracted using a power-law fitting routine [23].

4 Results

The atomic structure of the gate stack was recorded with the 300 keV STEM by simultaneous acquisition of HAADF and bright field (BF) images with the optical axis parallel to the [110] direction in Si. Representative pairs of HAADF and BF images are shown in Figs. 4a and b for the as-grown and the rapid-thermally annealed gate stacks, respectively. In the HAADF images the HfO_2 film appears in bright contrast due to the high atomic number of Hf ($Z = 72$) compared to Si ($Z = 14$). Typical Si dumbbell-like contrast is visible in the single-crystalline silicon substrate representing atomic columns 1.36 Å apart from each other. The amorphous SiO_2 interlayer reveals dark contrast in the HAADF images due to its amorphous character. However, the BF intensity shows a contrast pattern typical for amorphous SiO_2. The SiO_2 film thickness as determined from these images is consistent with a nominal thickness of 2 nm. After rapid thermal annealing

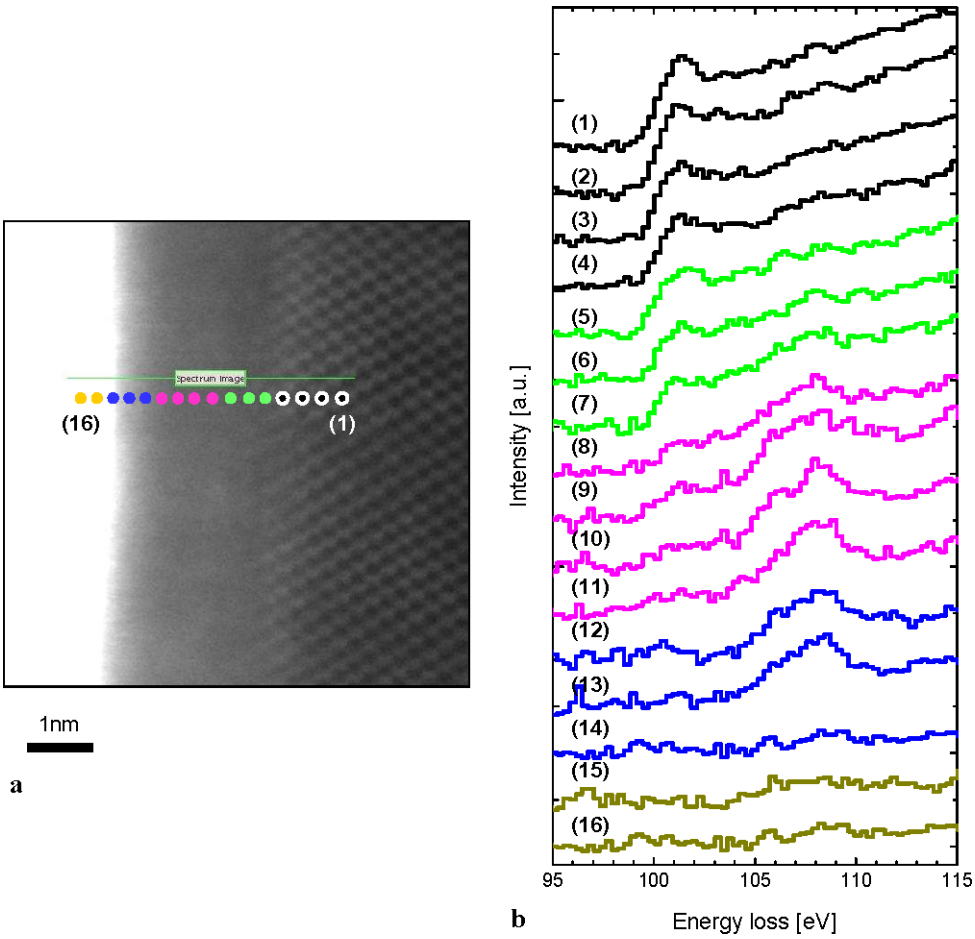

Fig. 6 HAADF survey image (**a**) after rapid thermal annealing, and EELS spectra of the Si $L_{2,3}$ absorption edge (**b**) recorded along the line identified in the survey image. All spectra were channel-to-channel gain corrected and background stripped

the HfO_2 film is poly-crystalline (Fig. 4b), while it remained amorphous in the as-grown stage (cf. Fig. 4a). The interlayer film thickness remains unchanged upon thermal annealing.

A more detailed inspection of the interlayer region reveals isolated bright contrast regions in the HAADF images inside the SiO_2 film of the annealed gate stack. No such regions were observed in the as-grown sample under similar imaging conditions and specimen thicknesses. Through-focal series acquisition revealed that these regions appear only in limited focus intervals and several different lateral and vertical positions inside the interlayer.

For both the as-grown and the thermally annealed gate stacks, energy-loss spectra of the Si $L_{2,3}$ absorption edge were recorded as line profiles perpendicular to the interface plane across the SiO_2 interlayer. For both samples, 20 spectra were recorded within approximately 4.7 nm, resulting in a spacing of roughly 2.35 Å per spectrum. The EELS analyses were conducted using the same TEM specimens and from the same specimen areas as the 3D imaging reported above. Figures 5 and 6 exhibit the results of the EELS investigations for the as-grown and the rapid thermally annealed interface structures, respectively. In Figs. 5a and 6a the survey HAADF images used to position the electron beam are shown, while Figs. 5b and 6b exhibit the acquired near-edge fine structures of the individual Si $L_{2,3}$ edge spectra acquired across the SiO_2 interlayer. The single spectra are numbered to identify the area they were recorded from in the corresponding survey images.

The near-edge fine structure changes quite abruptly as the probe is scanned across the gate stack for both the as-deposited and the annealed specimens, as shown in Figs. 5b and 6b. It was therefore possible to average different intervals of the EELS line traces to increase the signal-to-noise-ratios. The resulting EELS data are plotted in Fig. 7 for comparison of the near-edge fine structures. For the as-deposited case (scattered data), spectra 1–4, 5–8, 9–13, 14–16, and 17–20 were averaged and color-coded in black, green, purple, blue, and brown, respectively (cf. Fig. 5b). For the data recorded from the rapid thermal annealed sample (solid lines), spectra labeled 1–4, 5–7, 8–12, 13–14, and 15–16 in Fig. 6b were averaged and color-coded, respectively. Both samples show almost identical averaged EELS line shapes in the Si substrate (black), at the Si/SiO_2 interface (green), close to the SiO_2/HfO_2 interface (blue), and inside the HfO_2 film (brown). In the center of the SiO_2 interlayer (purple), however, the as-deposited sample exhibits

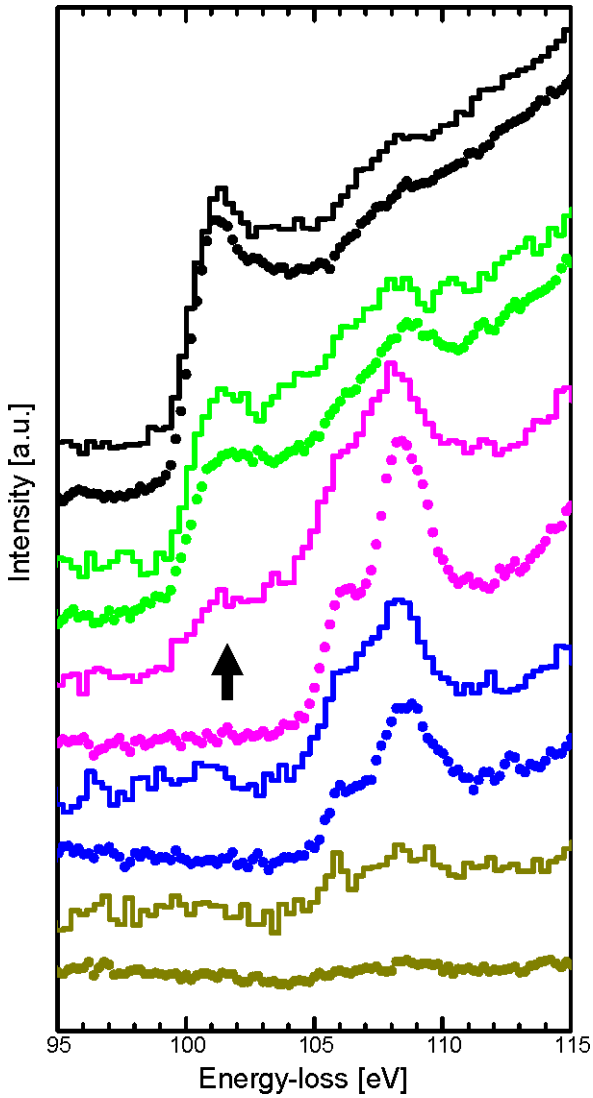

Fig. 7 Averaged EELS absorption edges for the as-deposited (*scattered lines*) and the annealed sample (*solid lines*). Spectra were averaged and color-coded according to their origin: *black* for the Si substrate; green at the SiO_2/Si interface; purple in the center of the SiO_2 film; blue at the HfO_2/SiO_2 interface; and brown in the HfO_2 film. Data adapted from [11]

Si $L_{2,3}$ near-edge fine structure typical for bulk SiO_2, while for the annealed interlayer, a significant additional spectral feature can be observed below the edge onset, highlighted by the arrow in Fig. 7.

5 Discussion

From the microstructure observations in Fig. 4 it is evident that the HfO_2 film crystallizes during the rapid thermal annealing process, which is typically used during CMOS device manufacturing as a dopant activation process [11]. However, a comparison of the HAADF images in Figs. 4a

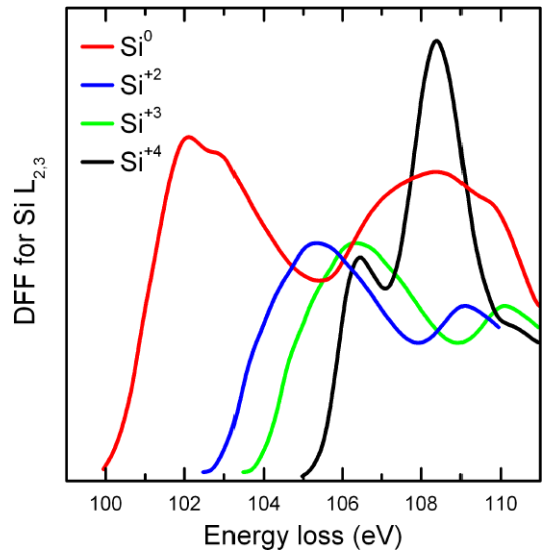

Fig. 8 Calculated dynamic form factors for the Si $L_{2,3}$ absorption edge for the most commonly found oxidation states, i.e., Si^0, Si^{+2}, Si^{+3}, and Si^{+4}

and b also indicates that isolated Hf atoms can be found within the SiO_2 interlayer after this rapid annealing process, while they were not detectable prior to the heat treatment at 1000°C for 10 s. Thus, it is the thermal activation process during CMOS manufacturing which is responsible for the incorporation of Hf atoms into the SiO_2 interlayer. In this study an Hf concentration of 0.3 ± 0.1 Hf atoms per cubic nanometer was observed. In a previous study concentrations as high as 1.4 ± 0.1 atoms per cubic nanometer were reported within an 8 Å thick chemical oxide [12, 13]. The diffusion coefficient for Hf in SiO_2 is only $D = 2.5 \times 10^{-18}$ cm^2/s at 1000°C, hence restricting Hf mobility under these conditions compared to a "*bad oxide*", i.e., oxygen deficient, in which a relatively increased number of oxygen vacancies will promote the diffusion process [11, 26, 27]. The resulting overall low density of Hf atoms observed in this study prevents the formation of Hf silicate since phase separation into crystalline HfO_2 and amorphous SiO_2 is thermodynamically favored [28]. The quality of the oxide, however, has a major influence on the diffusivity of Hf atoms into the interlayer. In this study, in accord with earlier observations [12, 29], also in a "*good oxide*" no Hf atoms were found to segregate to the Si/SiO_2 interface. In the survey images used for the EELS investigations the single Hf atoms observed in Fig. 4b are not that clearly resolved (cf. Fig. 6) due to a smaller sensitivity towards the detection of single atoms since for these measurements, the microscope was aligned with a high electron beam current setup limiting the spatial resolution of the 100 keV STEM to about 1.4 Å (unlike the setup chosen to acquire the micrograph shown in Fig. 2a).

The EELS results summarized in Fig. 7 demonstrate that the SiO_2 interlayer changes electronically after rapid ther-

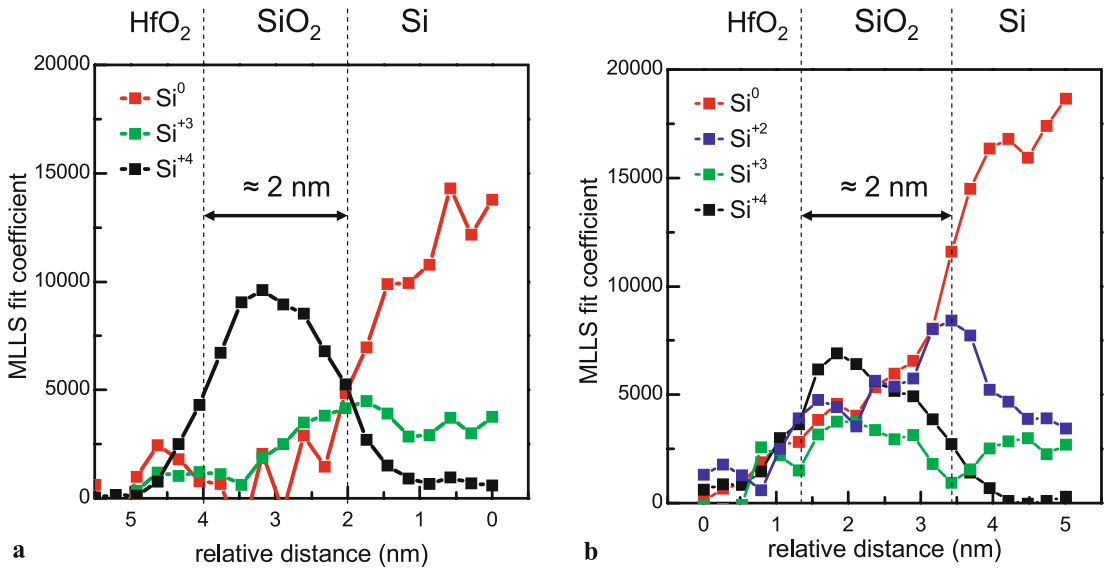

Fig. 9 Multiple linear least-squares fit coefficients for each EELS absorption edge recorded within line scans across the as-deposited (**a**) and the rapid thermally annealed interface structures (**b**). Error bars on the MLLS fit coefficients are approximately ±2000. The reference spectra in Fig. 8 were used for the fit routine

mal annealing only in the central region away from the interfaces with either the silicon substrate or the HfO_2. A nonzero spectral intensity below the edge onset typically indicates empty states in the band gap, most likely through the incorporation of oxygen vacancies. The following interpretation of these additional states is based on a set of calculated reference spectra of the Si $L_{2,3}$ edge for different valence states for Si^0, Si^{+2}, Si^{+3}, and Si^{+4} [30]. Figure 8 shows a plot of the calculated dynamic form factors kindly provided by Buczko. Calculational details for these spectra can be found in [30]. The energy scale for the calculated spectra was calibrated using X-ray photoelectron spectroscopy data following references [30, 31]. The spectra for atomic Si and Si^{+4} are in good agreement with the experimental spectra recorded from bulk Si and the SiO_2 film, respectively. The calculated reference spectra were used for multiple linear least-squares (MLLS) fitting of each of the spectra of both EEL line profiles plotted in Figs. 5 and 6. Fitting was perfomed using the Gatan Digital Micrograph software package [32]. The resulting MLLS fitting coefficients are plotted in Fig. 9 as a function of relative distance across the interface structures for both the as-deposited and the fully processed samples. The Si $L_{2,3}$ edge for the SiO_2 interlayer in the as-deposited sample is reproduced solely by the reference spectrum for Si^{+4}, as can be expected for a thermally grown "*good oxide*" with SiO_2 composition. The full-width half maximum of the corresponding MLLS coefficients across the interlayer is about 2 nm, re-confirming the nominal oxide thickness and showing that drift correction during EELS measurements was successful. In the area of the Si substrate the MLLS coefficients for Si^0 dominate the fit, while a small amount of Si^{+3} can be observed, which is most likely due to surface oxidation of the TEM sample. No significant evidence above the noise level (i.e., ±2000 in Fig. 9) was found for any presence of the Si^{+2} valence state in the as-grown gate stack. For the fully processed interface structure, i.e., after rapid thermal annealing, the valence contributions change. In the area of the Si substrate the fitting results remain unchanged, and only MLLS coefficients for Si^0 and Si^{+3} are found. However, the spectra recorded from the interlayer are best fitted by a superposition of Si^{+4} and Si^{+2} valence states as well as a small contribution from Si^{+3} valence states. Reduction of the SiO_2 interlayer occurred during the annealing process, generating an increased number of oxygen vacancies inside the former SiO_2 interlayer. This formation of oxygen vacancies will then increase the diffusion coefficient for Hf atoms in the interlayer, which then correlates with the single atom imaging results reported above. These results are consistent with earlier reports of the same interface structures by Bersuker et al. [11], who confirmed oxygen removal from the SiO_2 film due to HfO_2 deposition using electron spin resonance spectroscopy. The assignment of point defect configurations in the interlayer, such as P_b or E' centers, is beyond the scope of this study since EELS data obtained with both higher spatial and energy resolution are necessary for proper quantification.

6 Summary and conclusions

Aberration-corrected STEM is a very powerful tool for the atomic scale characterization of semiconductor interfaces.

Combining STEM imaging with single atom sensitivity in all three dimensions and energy-loss spectroscopy provides detailed information about the atomic and electronic structure of, as shown here, high-*k* dielectric interfaces.

In this systematic study of a $HfO_2/SiO_2/Si$ gate stack, a small number of single Hf atoms were detected inside the thermally grown SiO_2 interlayer after rapid thermal annealing but not in the as-grown state. In combination with quantitative EELS analysis of the near-edge fine structures of the Si $L_{2,3}$ absorption edges, it was found that the rapid thermal annealing process during device manufacturing incorporates oxygen vacancies into the SiO_2 interlayer. This effect increases the diffusion of single Hf atoms into the interlayer. The so formed point defect structures generate band gap states in the interlayer, which can act as charge traps, and decrease electron mobilities along the gate channel [11]. Since the Hf atom densities in this study are by a factor of 4–5 smaller than observed in a chemically grown oxide [12], it can further be concluded that the quality of the Si–O interlayer has a major impact on interdiffusion between the high-*k* dielectric film and the silicon oxide.

Acknowledgements The authors acknowledge fruitful discussions and collaborations with S.T. Pantelides, R. Buczko, G. Bersuker, and B. Foran, and excellent TEM specimen preparation by J.T. Luck. K.v.B. appreciates partial funding through a Feodor-Lynen scholarship from the Alexander-von-Humboldt Foundation. This research was funded by the Division of Materials Sciences and Engineering (S.J.P.) and the Division of Scientific User Facilities (K.v.B.) of the US Department of Energy at Oak Ridge National Laboratory, which is operated by UT-Battelle, LLC.

References

1. G. Moore, Electronics **38**, 00 (1965)
2. P.A. Packan, Science **285**, 2079 (1999)
3. M. Varela, A.R. Lupini, K. van Benthem, A.Y. Borisevich, M.F. Chisholm, N. Shibata, E. Abe, S.J. Pennycook, Annu. Rev. Mater. Res. **35**, 539 (2005)
4. P.E. Batson, N. Dellby, O.L. Krivanek, Nature **418**, 617 (2002)
5. P.D. Nellist, M.F. Chisholm, N. Dellby, O.L. Krivanek, M.F. Murfitt, Z.S. Szilagyl, A.R. Lupini, A.Y. Borisevich, W.H. Sides, S.J. Pennycook, Science **305**, 1741 (2004)
6. S. Wang, A.Y. Borisevich, S.N. Rashkeev, K. Sohlberg, M.V. Glazoff, S.J. Pennycook, S.T. Pantelides, Nat. Mater. **3**, 143 (2004)
7. H.R. Huff, D.C. Gilmer (eds.), *High dielectric Constant Materials* (Springer, Berlin, 2005)
8. Y.-S. Lin, R. Puthenkovilakam, J.P. Chang, C. Bouldin, I. Levin, N.V. Nguyen, J. Ehrstein, Y. Sun, P. Pianetta, T. Conard, W. Vandervorst, V. Venturo, S. Selbrede, J. Appl. Phys. **93**, 5945 (2003)
9. G. Bersuker, J. Barnett, N. Moumen, B. Foran, C.D. Young, P. Lysaght, J. Peterson, B.H. Lee, P.M. Zeitzoff, H.R. Huff, Jpn. J. Appl. Phys. **43**, 7899 (2004)
10. D. Chi, P.C. McIntyre, Appl. Phys. Lett. **85**, 4699 (2004)
11. G. Bersuker, C.S. Park, J. Barnett, P.S. Lysaght, P.D. Kirsch, C.D. Young, R. Choi, B.H. Lee, B. Foran, K. van Benthem, S.J. Pennycook, P.M. Lenahan, J.T. Ryan, J. Appl. Phys. **100**, 094108 (2006)
12. K. van Benthem, A.R. Lupini, M. Kim, H.S. Baik, S.J. Doh, J.-H. Lee, M.P. Oxley, S.D. Findlay, L.J. Allen, S.J. Pennycook, Appl. Phys. Lett. **87**, 034104 (2005)
13. K. van Benthem, A.R. Lupini, M.P. Oxley, S.D. Findlay, L.J. Allen, S.J. Pennycook, Ultramicroscopy **106**, 1062 (2006)
14. P.E. Batson, Microsc. Microanal. **11**(2), 2124 (2005)
15. M.P. Agustin, L.R.C. Fonseca, J.C. Hooker, S. Stemmer, Appl. Phys. Lett. **87**, 121909 (2005)
16. D.O. Klenov, T.E. Mates, S. Stemmer, Appl. Phys. Lett. **89**, 041918 (2006)
17. O.L. Krivanek, P.D. Nellist, N. Dellby, M.F. Murfitt, Z. Szilagyi, Ultramicroscopy **96**, 229 (2003)
18. K. van Benthem, S.N. Rashkeev, S.J. Pennycook, in *Characterization and Metrology for ULSI Technology*, ed. by D.G. Seiler, A.C. Diebold, R. McDonald, C.R. Ayre, R.P. Khosla, S. Zollner, E.M. Secula. American Institute of Physics Conference Proceedings, vol. 788 (2005), p. 79
19. A.R. Lupini, S.J. Pennycook, Ultramicroscopy **96**, 313 (2005)
20. A.Y. Borisevich, A.R. Lupini, S.J. Pennycook, Proc. Natl. Acad. Sci. **103**, 3044 (2006)
21. P.A. Midgley, M. Weyland, Ultramicroscopy **96**, 413 (2003)
22. I. Arslan, T.J.V. Yates, N.D. Browning, P.A. Midgley, Science **309**, 2195 (2005)
23. R.F. Egerton, *Electron Energy Loss Spectroscopy in the Electron Microscope*, 2nd edn. (Plenum Press, New York, 1996)
24. H. Kohl, H. Rose, Adv. Imaging Electron Phys. **65**, 173 (1985)
25. A. Strecker, U. Bäder, M. Kelsch, U. Salzberger, M. Sycha, M. Gao, G. Richter, K. van Benthem, Z. Metallkd. **94**, 290 (2003)
26. J.C. Lee, S.J. Oh, M.J. Cho, C.S. Hwang, R.J. Jung, Appl. Phys. Lett. **84**, 1305 (2004)
27. P.S. Lysaght, G. Bersuker, J.J. Peterson, C.D. Young, P. Majhi, B.-H. Lee, H.R. Huff, Appl. Phys. Lett. **87**, 082903 (2005)
28. N. Ikarashi, K. Watanabe, K. Masuzaki, T. Nakagawa, Appl. Phys. Lett. **88**, 101912 (2006)
29. A. Marinopulos, K. van Benthem, S.N. Rashkeev, S.J. Pennycook, S.T. Pantelides, Phys. Rev. Lett. **77**, 195317 (2008)
30. R. Buczko, G. Duscher, S.J. Pennycook, S.T. Pantelides, Phys. Rev. Lett. **85**, 2168 (2000)
31. M.L. Green, E.P. Gusev, R. Degraeve, E.L. Garfunkel, J. Appl. Phys. **90**, 2057 (2001)
32. Gatan Inc., 5794 W. Las Positas Blvd., Pleasanton, CA 94588, USA. www.gatan.com